

Sampling Innovation-Based Adaptive Compressive Sensing

Zhifu Tian, Tao Hu*, Chaoyang Niu, Di Wu, Shu Wang
Information Engineering University, Zhengzhou, China

tzhifu@qq.com, hutaoengineering@163.com, niucy2017@outlook.com,
wudipaper@sina.com, shu1008@mail.ustc.edu.cn

Abstract

Scene-aware Adaptive Compressive Sensing (ACS) has attracted significant interest due to its promising capability for efficient and high-fidelity acquisition of scene images. ACS typically prescribes adaptive sampling allocation (ASA) based on previous samples in the absence of ground truth. However, when confronting unknown scenes, existing ACS methods often lack accurate judgment and robust feedback mechanisms for ASA, thus limiting the high-fidelity sensing of the scene. In this paper, we introduce a Sampling Innovation-Based ACS (SIB-ACS) method that can effectively identify and allocate sampling to challenging image reconstruction areas, culminating in high-fidelity image reconstruction. An innovation criterion is proposed to judge ASA by predicting the decrease in image reconstruction error attributable to sampling increments, thereby directing more samples towards regions where the reconstruction error diminishes significantly. A sampling innovation-guided multi-stage adaptive sampling (AS) framework is proposed, which iteratively refines the ASA through a multi-stage feedback process. For image reconstruction, we propose a Principal Component Compressed Domain Network (PCCD-Net), which efficiently and faithfully reconstructs images under AS scenarios. Extensive experiments demonstrate that the proposed SIB-ACS method significantly outperforms the state-of-the-art methods in terms of image reconstruction fidelity and visual effects. Codes are available at https://github.com/giant-pandada/SIB-ACS_CVPR2025.

1. Introduction

Compressive Sensing (CS) leverages the sparsity of signals, utilizing under-sampled bases for measurements to reconstruct the original signals with maximum fidelity. This technique has found broad application in various fields, including terahertz imaging [56], hyperspectral imaging [25],

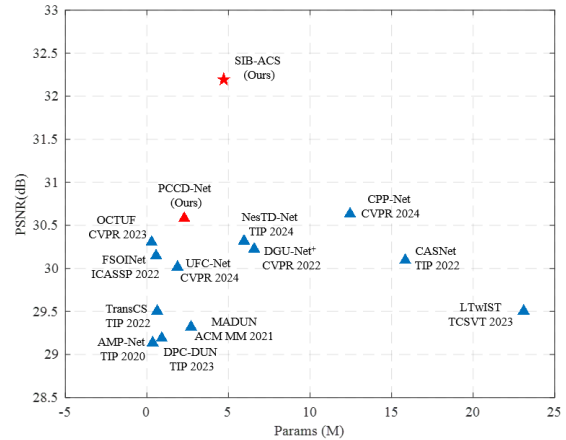


Figure 1. Comparison of average PSNR performance at the sampling rates of 0.10 and 0.25 on the BSD68 [37] and Urban100 [33] datasets between the proposed ACS model SIB-ACS, UCS model PCCD-Net and the state-of-the-art CS methods.

Magnetic Resonance Imaging (MRI) [32], and underwater imaging [82]. The Uniform Compressive Sensing (UCS) [31, 62] model employs a uniform sampling rate across each image block for sample acquisition, followed by image reconstruction. However, due to the regional complexity variations often found in real-world images, areas of higher complexity require more extensive sampling for effective recovery. Adaptive Compressive Sensing (ACS) [14, 27, 44, 80] addresses this by dynamically adjusting the sampling allocation based on the content of individual image blocks, thereby enhancing the efficiency of scene sensing. ACS has been widely adopted in areas such as single-pixel imaging [30, 49], image encryption [20, 48], video compressive sensing [61, 64], and medical imaging [38].

The most significant challenge for ACS is to perform adaptive sampling allocation (ASA) across various complex image regions, particularly in the absence of ground truth. When the ground truth is unavailable, existing ACS frameworks typically employ two-stage [28, 76] or multi-stage [14, 27, 43, 44] sampling, utilizing the sampling information from all previous stages. Multi-stage sampling

*Corresponding authors.

holds immense potential as it iteratively reduces ASA errors through feedback mechanisms. When determining ASA, existing ACS methods analyze the previous measurements or the content of reconstructed images, allocating more samples to regions with larger measurement errors [28, 43, 66], higher cosine similarity in measurements [63], higher measurement scores [44], or more complex content in reconstructed images [60, 71]. However, existing ACS methods carry a potential risk of ASA errors. For methods in the measurement domain, the under-sampled measurement data are intrinsically more ill-posed than image data, leading to a significant potential for ASA errors. For methods in the image domain, the associated analysis indicators form a positive feedback loop with the sampling, which tends to concentrate sampling to the area of initial allocation [43], ultimately constraining the imaging capability of ACS.

To address the aforementioned issues, this paper proposes a Sampling Innovation-Based Adaptive Compressive Sensing (SIB-ACS) framework, which utilizes incremental image information from historical sampling and sampling increments to determine ASA through a multi-stage negative feedback process. Specifically, the proposed framework allocates sampling resources based on the size of the recovery of the principal components in the sampling increment, which we refer to as sampling innovation (SI). Furthermore, to fully harness SI in guiding adaptive sampling (AS), we have developed a multi-stage SI-guided AS model that corrects the ASA errors stage by stage in a negative feedback manner. For image reconstruction, we have designed a computationally efficient Principal Component Compressed Domain Network (PCCD-Net) to reconstruct high-fidelity images from adaptive sampling values. The proposed PCCD-Net employs proximal gradient descent (PGD) operations in the principal component (PC) image to compress the dimensions of PGD operations in the feature domain (FD), and simultaneously uses the PGD in the compressed FD to supplement the details of the features in the results of PGD in the PC image. As illustrated in Fig. 1, the proposed SIB-ACS adaptively senses the scenario, significantly outperforming the state-of-the-art CS methods. The main contributions are summarized as follows:

- We propose a SIB-ACS framework that utilizes incremental image information from historical sampling and sampling increments to determine ASA, thereby enhancing the accuracy of ASA and achieving high-fidelity image reconstruction.
- We design a SI-guided multi-stage ASA model, which accomplishes multi-stage ASA at any sampling rate with a single model, facilitated by an image domain negative feedback mechanism.
- We introduce a PCCD-Net for image reconstruction in ACS scenarios, which leverages PGD operations in the

PC image to compress the dimensions of PGD in the FD features, thereby significantly reducing the computational cost while maintaining high image reconstruction performance.

- Extensive experiments demonstrate that the proposed SIB-ACS significantly outperforms the state-of-the-art CS methods.

2. Related work

Adaptive Compressive Sensing Methods. ACS dynamically allocates sampling rates based on the complexity of block image content, thereby enhancing image sensing capabilities. On the one hand, when scene images are available, existing studies have achieved significant results by guiding AS based on scene content analysis indicators such as texture [42, 60], edge [36, 56, 57], entropy [81], variance [61, 64], gradient [42], wavelet components [1, 13, 25, 49, 70], energy [39, 40, 82], or saliency distribution [2, 71]. On the other hand, when scenes are unknown, existing studies employ two-stage [28, 76] or multi-stage models [14, 27, 43, 44] for AS, using the sampling from all previous AS stages to make ASA judgments. Generally, ASA methods include measurement domain (MD) and image domain (ID) methods. Specifically, existing MD methods use measurement value-related indicators for ASA, allocating more samples to areas with high indicators such as scene measurement error [28, 43, 66], cosine similarity in measurements [63], and network scores of measurements [44]. In addition, ID methods [76] first reconstruct all previous sampling values into preliminary images, then allocate more samples to areas with high analysis indicators in the content of the preliminary reconstructed images. These ASA methods have achieved significant results by distinguishing image regions using different strategies [43, 76].

However, when the scene is unknown, the ASA results of existing ACS methods fall short of the ideal effect. MD methods tend to have noticeable judgment errors due to the inherent ill-posedness of under-sampled measurement data in comparison to image data. In ID methods, the sampling and image analysis indicators form a positive feedback loop, making it difficult to correct ASA errors in the multi-stage ACS framework [43], resulting in its accuracy heavily relying on the initial reconstructed image quality, which often degrades significantly under low sampling conditions. These limitations in existing ASA methods have hindered the imaging performance of ACS to varying degrees in terms of ASA accuracy, obstructing the practical application of high-fidelity ACS. For unknown scenes, we propose a SIB-ACS method that utilizes all historical sampling and sampling increment information to implement an image-level negative feedback multi-stage AS framework.

CS Reconstruction Networks. Leveraging the success of

machine vision [21, 22], image CS has developed purely deep learning-based (purely DL) networks and deep unfolding networks (DUNs). Purely DL methods utilize the mapping capabilities of neural networks to learn the inverse problem of image reconstruction, resulting in pure CNN networks [15, 16, 46, 47, 68, 79], attention-based networks [17], and hybrid networks of CNN and Transformer [11, 15, 29, 50, 59, 69] for CS. Purely DL networks improve the capabilities for block artifact removal and image denoising by harnessing the networks’ mapping abilities but suffer from the infamous black box problem. On the other hand, DUNs integrate traditional optimization algorithms with neural networks, enhancing image reconstruction performance by using the networks’ robust mapping capabilities and injecting measurement physics information [74]. Researchers have extensively explored the networks that unfold various traditional optimization algorithms [4, 12, 23, 31, 58, 62, 67, 72]. Notably, it is proven that large dimensions of physics measurement injection [3, 5, 9, 26, 35, 73, 76] and information flow [6, 10, 34, 41, 51, 54] can further enhance DUNs’ performance. However, a large physics injection dimension usually implies higher computational cost, such as for gradient descent (GD) operations. Particularly compared to UCS, ACS requires more sampling in complex areas, leading to a larger physics injection computational costs due to the increased sampling matrix. In this paper, we introduce a PCCD-Net for ACS, which uses the principal component GD to compress the dimensionality of the feature domain GD, thereby achieving high image fidelity with fewer operations.

3. Proposed method

In this section, we provide a detailed introduction to the proposed SIB-ACS, which includes an adaptive sampling module (ASM) and an image reconstruction module, as depicted in Figs. 2 and 3, respectively.

3.1. ASM

Innovation Criterion. ACS optimizes the sampling strategy with the objective function of minimizing the error in the reconstructed image. Accordingly, when the ground truth is unavailable, we design an innovation method to allocate the sampling resources based on the image successfully reconstructed from historical sampling values. Specifically, innovation refers to the increase in the components of the reconstructed image or the decrease in the reconstruction error that results from an increase in the sampling rate. The sampling used to measure the innovation is referred to as innovation sampling. In detail, innovation can be defined as

$$\alpha = \|\hat{\mathbf{x}}_{\text{IS}} - \hat{\mathbf{x}}_{\text{HM}}\|_2^2 = \|(\mathbf{x} - \hat{\mathbf{x}}_{\text{HM}}) - (\mathbf{x} - \hat{\mathbf{x}}_{\text{IS}})\|_2^2, \quad (1)$$

where $\hat{\mathbf{x}}_{\text{HM}}$ represents the image reconstructed from the historical measurements, $\hat{\mathbf{x}}_{\text{IS}}$ denotes the image reconstructed

after innovation sampling, and \mathbf{x} is the original image. The innovation method adaptively determines the number of samples for each image block, based on the magnitude of the innovation within the same image. With this method, the adaptively allocated number of samples can be expressed as

$$M_n = M_{\text{ASR}} \frac{\|\alpha_n\|_2^2}{\sum_n \|\alpha_n\|_2^2}, \quad (2)$$

where M_{ASR} denotes the adaptive sampling resources, while α_n and M_n represent the innovation and the adaptively allocated sample count for the n -th image block, respectively. As illustrated by Eq. (1), innovation is a direct estimation of the decrease in reconstruction error. Therefore, the direction guided by innovation-based AS aligns with the goal of reducing the image reconstruction error, ensuring that the AS progresses towards minimizing the total image reconstruction error. Furthermore, innovation is a relative measure, not an absolute one. As the number of samples guided by innovation within an image block increases, the innovation will gradually decrease once the principal components of the image are restored, which creates a negative feedback mechanism, guiding AS towards a larger recovery of innovation, thereby enabling the possibility of multi-stage AS at the image level.

Innovation-guided ASM. The innovation-guided multi-stage ASM comprises two stages: the initial sampling stage and the multi-stage AS stage, as illustrated in Fig. 2.

The initial sampling stage acts as the startup stage of the ASM. For all image blocks, a uniform initial sampling count M_{init} or sampling rate SR_{init} is employed to acquire the initial sampling values. Therefore, the initial sampling stage can be expressed as

$$\mathbf{y}_{1:M_{\text{init}}} = \mathbf{A}_{1:M_{\text{init}}}\mathbf{x}, \quad (3)$$

where $\mathbf{A}_{1:M_{\text{init}}}$ and $\mathbf{y}_{1:M_{\text{init}}}$ respectively denote the initial sampling matrix and the initial sampling values with a sample count of M_{init} .

The multi-stage AS stage effectively leverages the multi-stage negative feedback mechanism to progressively eliminate the residual innovation in each block image. Specifically, each AS stage involves three steps: Innovation Sampling (IS), Innovation Estimation (IE), and Adaptive Sampling (AS), as depicted in Fig. 2(a). Particularly, the first step, IS, is based on the sampling distribution at the $s - 1$ -th stage, conducting uniform sampling with a sample count of M_{IS} or a sampling rate of SR_{IS} , to uniformly probe the innovation distribution. Therefore, IS at the s -th stage can be represented as

$$\mathbf{y}_{1:M_{\text{IS},s}} = \mathbf{A}_{1:M_{\text{IS},s}}\mathbf{x}, \quad (4)$$

where $\mathbf{A}_{1:M_{\text{IS},s}}$ and $\mathbf{y}_{1:M_{\text{IS},s}}$ respectively denote the IS matrix and the IS values with a sample count of M_{IS} at the

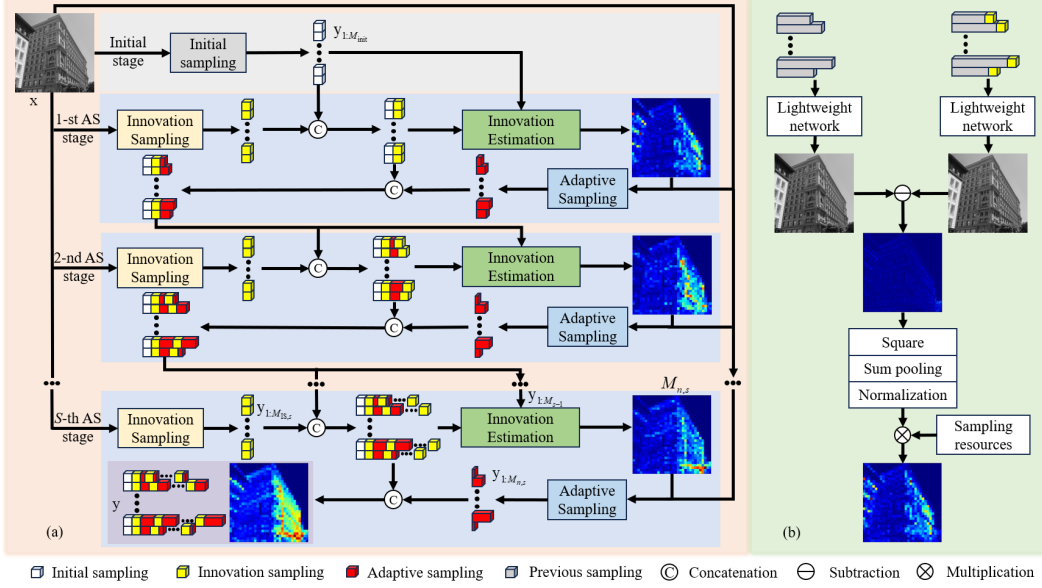


Figure 2. The overview of the proposed sampling innovation-based ASM. (a) Innovation-guided multi-stage AS, (b) Innovation Estimation (IE) based on the reconstructed image information from sampling values before and after Innovation Sampling (IS).

s -th stage. The sampling values $\mathbf{y}_{1:M_{s-1}+M_{IS,s}}$ after the IS at the s -th stage are formed by concatenating the sampling value of pre- $s-1$ stage $\mathbf{y}_{1:M_{s-1}}$ and $\mathbf{y}_{1:M_{IS,s}}$, and the sampling matrix $\mathbf{A}_{1:M_{s-1}+M_{IS,s}}$ is formed by concatenating $\mathbf{A}_{1:M_{s-1}}$ and $\mathbf{A}_{1:M_{IS,s}}$.

Subsequently, as shown in Fig. 2(b), the second step, IE at the s -th stage, initially employs lightweight networks to swiftly reconstruct the images $\hat{\mathbf{x}}_{s-1}$ and $\hat{\mathbf{x}}_{IS,s}$ before and after the IS, respectively,

$$\hat{\mathbf{x}}_{s-1} = \mathcal{F}_{s_1}(\mathbf{y}_{1:M_{s-1}}, \mathbf{A}_{1:M_{s-1}}), \quad (5)$$

$$\hat{\mathbf{x}}_{SI,s} = \mathcal{F}_{s_2}(\mathbf{y}_{1:M_{s-1}+M_{IS,s}}, \mathbf{A}_{1:M_{s-1}+M_{IS,s}}), \quad (6)$$

where \mathcal{F}_{s_1} and \mathcal{F}_{s_2} respectively denote the lightweight reconstruction networks before and after IS. Subsequently, the innovation at the s -th stage can be computed according to Eq. (1),

$$\alpha_s = \|\hat{\mathbf{x}}_{IS,s} - \hat{\mathbf{x}}_{s-1}\|_2^2. \quad (7)$$

Next, the innovation across the entire image is normalized to derive the weight $\frac{\|\alpha_n\|_2^2}{\sum_n \|\alpha_n\|_2^2}$ for block image sampling allocation. Additionally, in the multi-stage AS process, an image with height H and width W respectively, is divided into N block images of size B . The total sampling resource that can be allocated at each AS stage of the S -stage ASM, given a total sampling rate of SR , is computed as $M_{ASR,s} = \lceil \frac{H}{B} \rceil \lceil \frac{W}{B} \rceil B^2 (\frac{SR - SR_{init}}{S} - SR_{IS})$, where $\lceil \cdot \rceil$ denotes the operation of taking the ceiling. Therefore, the number of adaptive samples for the n -th image block at the s -th stage is

$$M_{n,s} = M_{ASR,s} \frac{\|\alpha_{n,s}\|_2^2}{\sum_n \|\alpha_{n,s}\|_2^2}. \quad (8)$$

In the third step, AS is applied to the image, utilizing the adaptive sampling count for the n -th image block in the s -th stage, as determined in the second step. The maximum full sampling rate is assumed to be 1 by default, so we set the maximum sampling rate of each image block after the AS in the s -th stage to be s/S . Upon completion of the s -th stage AS, the sampling values $\mathbf{y}_{1:M_s}$ from the preceding s stages are obtained by concatenating $\mathbf{y}_{1:M_{s-1}+M_{IS,s}}$ and $\mathbf{y}_{1:M_{n,s}}$.

This AS process is iterated across S stages, ultimately yielding the final sampling value \mathbf{y} from the ASM.

3.2. PCCD-Net for image reconstruction

The Principal Component Compressed Domain Network (PCCD-Net) is depicted in Fig. 3. Firstly, the initial reconstructed image is generated through the deconvolution of the adaptive sampling values and the corresponding sampling matrix,

$$\mathbf{x}^0 = \mathbf{A}^T \mathbf{y}, \quad (9)$$

where \mathbf{A}^T represents the transpose of \mathbf{A} . Subsequently, the initial reconstructed image is transformed into initial features with C channels,

$$\mathbf{X}^0 = \text{Conv}_{12F}(\mathbf{x}^0), \quad (10)$$

where Conv_{12F} denotes the convolution operation that transforms the image to features. Next, the initial features are updated to the final reconstructed features through K phases of Proximal Gradient Descent (PGD) [8] iteration. Specifically, each iterative stage is divided into a Principal Component PGD (PCPGD) path and a Compressed Domain PGD (CDPGD) path, as shown in Fig. 3(b) and Fig. 3(c), respectively. The PCPGD first aggregates the reconstructed

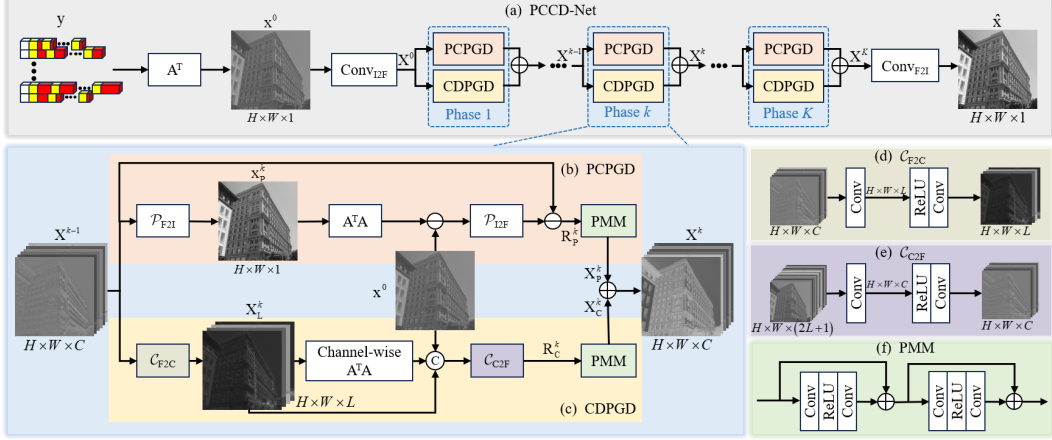


Figure 3. The overview of the proposed PCCD-Net for image reconstruction. (a) Deep reconstruction process, (b) PCPGD path, (c) CDPGD path, (d) Convolutional block that transitions features from the FD to the CD, (e) Convolutional block that transitions features from the CD back to the FD, (f) Proximal Mapping Module (PMM).

features from the previous stage into a principal component (PC) image through a convolution operation. Subsequently, the PCPGD calculates the gradient of the PC image and uses a convolution operation to extend the gradient image back into the feature domain (FD), where the proximal mapping operation is executed. The PCPGD process can be represented as follows:

$$\mathbf{x}_p^k = \mathcal{P}_{F2I}(\mathbf{X}^{k-1}), \quad (11)$$

$$\mathbf{R}_p^k = \mathbf{X}^{k-1} - \mathcal{P}_{I2F}(\mathbf{A}^T(\mathbf{A}\mathbf{x}_p^k - \mathbf{y})), \quad (12)$$

$$\mathbf{X}_p^k = \mathcal{F}_{PM}(\mathbf{R}_p^k), \quad (13)$$

where \mathbf{x}_p^k and \mathbf{X}_p^k respectively represent the PC image and features at the k -th phase, while \mathcal{P}_{I2F} and \mathcal{P}_{F2I} denote the convolution operations that transition from the PC image to features and from features back to the PC image, respectively. \mathcal{F}_{PM} stands for the proximal mapping module (PMM), as shown in Fig. 3(f). The CDPGD integrates the reconstructed features from the previous stage into compressed domain (CD) complementary features of dimension L via a convolution block, and then computes the gradient in a channel-wise manner. Subsequently, the gradient descent process is completed by executing a convolution block operation following concatenating features of different dimensions. Finally, the CD gradient is restored to the FD of dimension C , where the PMM is implemented. The CDPGD process can be represented as:

$$\mathbf{X}_L^k = \mathcal{C}_{F2C}(\mathbf{X}^{k-1}), \quad (14)$$

$$\mathbf{R}_c^k = \mathcal{C}_{C2F}(\text{Concat}(\mathbf{X}_L^k, \mathbf{A}^T \mathbf{A} \mathbf{X}_L^k, \mathbf{A}^T \mathbf{y})), \quad (15)$$

$$\mathbf{X}_c^k = \mathcal{F}_{PM}(\mathbf{R}_c^k), \quad (16)$$

where \mathbf{x}_c^k and \mathbf{X}_L^k denote the CD image and features at the k -th phase, respectively. Meanwhile, \mathcal{C}_{F2C} and \mathcal{C}_{C2F} respectively represent the convolutional operations that transition features from the FD to the CD and from the CD

back to the FD, as shown in Fig. 3(d) and Fig. 3(e), respectively. At this point, the image features updated by both PCPGD and CDPGD are amalgamated in a complementary fashion, culminating in the comprehensive image features $\mathbf{X}^k = \mathbf{X}_p^k + \mathbf{X}_c^k$. Ultimately, following K phases of iterative update, the comprehensive image features are aggregated via a convolution operation to yield the reconstructed image,

$$\hat{\mathbf{x}} = \text{Conv}_{F2I}(\mathbf{X}^K), \quad (17)$$

where Conv_{F2I} represents the convolution operation that transitions from features to the image.

3.3. Loss Function

Considering the quality of both the reconstructed image pixels and textures in the SIB-ACS, we employ a combined loss function consisting of l_1 loss and SSIM loss [69, 78], expressed as follows:

$$\mathcal{L}(\Theta) = \mathcal{L}_{l_1}(\Theta) + \mu \mathcal{L}_{SSIM}(\Theta), \quad (18)$$

where Θ represents all the learnable parameters of the model, \mathcal{L}_{l_1} and \mathcal{L}_{SSIM} represent l_1 loss and SSIM loss, respectively, and μ is an empirical constant.

4. Experiments

4.1. Experimental Settings

In the SIB-ACS, we set the block size B for the image to 32, and the initial sampling rate SR_{init} is defined to 0.02. Empirically, we determine the innovation sampling rate SR_{IS} as $\frac{SR - SR_{\text{init}}}{2S}$, set the number of AS stages S to 4 [43, 44], and set μ to 0.1 [44]. The number of channels between iterative phases in the PCCD-Net is set to 32 [55] and the dimension of the compressed domain is defined to 4. The number of phases K in the PCCD-Net is set to 24. More

Table 1. Average PSNR (dB) and SSIM results of recent uniform and adaptive CS methods on BSD68 [37] and Urban100 [33] with different sampling ratios. The best and second-best results are marked in red and blue colors, respectively.

Dataset	Models		CS Ratio					Average
			SR = 0.10	SR = 0.25	SR = 0.30	SR = 0.40	SR = 0.50	
BSD68	Uniform Sampling	AMP-Net-9-BM (TIP 2021) [77]	27.86/0.7926	31.74/0.9048	32.84/0.9240	34.86/0.9508	36.82/0.9680	32.82/0.9080
		MADUN (ACM MM 2021) [52]	26.83/0.7620	30.81/0.8845	31.87/0.9068	33.81/0.9376	35.76/0.9582	31.82/0.8898
		TransCS (TIP 2022) [45]	27.86/0.8086	31.74/0.9121	32.56/0.9276	34.82/0.9540	36.81/0.9699	32.76/0.9144
		FSOINet (ICASSP 2022) [7]	28.27/0.8187	32.21/0.9183	33.29/0.9348	35.32/0.9577	37.34/0.9727	33.29/0.9204
		DGUNet ⁺ (CVPR 2022) [41]	28.13/0.8165	31.97/0.9158	-/-	-/-	37.04/0.9718	-/-
		LTWIST (TCSVT 2023) [18]	27.85/0.8082	31.64/0.9102	-/-	-/-	-/-	-/-
		DPC-DUN (TIP 2023) [53]	26.77/0.7608	30.70/0.8832	31.75/0.9050	33.70/0.9364	35.62/0.9574	31.71/0.8886
		OCTUF (CVPR 2023) [55]	28.28/0.8177	32.24/0.9185	33.32/0.9348	35.35/0.9578	37.41/0.9729	33.32/0.9203
		NesTD-Net (TIP 2024) [19]	28.28/0.8231	32.30/0.9203	33.22/0.9354	35.37/0.9586	-/-	-/-
		UFC-Net (CVPR 2024) [65]	27.95/0.8086	31.74/0.9093	-/-	-/-	-/-	-/-
		CPP-Net (CVPR 2024) [24]	28.41/0.8227	32.25/0.9188	33.34/0.9353	35.33/0.9575	37.30/0.9722	33.33/0.9213
		CASNet (TIP 2022) [2]	28.41/0.8230	32.31/0.9196	33.39/0.9358	35.44/0.9581	37.49/0.9728	33.41/0.9219
		AMS-Net (TMM 2022) [75]	29.36/0.8073	33.53/0.9146	34.67/0.9321	36.88/0.9555	39.20/0.9703	34.73/0.9160
		Uformer-ICS (TSC 2023) [76]	27.75/0.7978	31.74/0.9006	32.62/0.9179	34.15/0.9425	35.49/0.9590	32.35/0.9036
SIB-ACS (ours)	29.54/0.8401	34.35/0.9312	35.72/0.9455	38.38/0.9653	41.14/0.9779	35.83/0.9320		
Urban100	Uniform Sampling	AMP-Net-9-BM (TIP 2021) [77]	26.03/0.8148	30.87/0.9199	32.18/0.9363	34.35/0.9577	36.31/0.9710	31.95/0.9199
		MADUN (ACM MM 2021) [52]	27.11/0.8389	32.52/0.9344	33.74/0.9469	35.72/0.9630	37.70/0.9744	33.36/0.9315
		TransCS (TIP 2022) [45]	26.72/0.8411	31.70/0.9329	31.95/0.9382	35.20/0.9647	37.18/0.9760	32.55/0.9306
		FSOINet (ICASSP 2022) [7]	27.53/0.8624	32.60/0.9428	33.82/0.9538	35.90/0.9686	37.77/0.9775	33.52/0.9410
		DGUNet ⁺ (CVPR 2022) [41]	28.01/0.8707	32.76/0.9450	-/-	-/-	37.63/0.9783	-/-
		LTWIST (TCSVT 2023) [18]	26.76/0.8461	31.78/0.9347	-/-	-/-	-/-	-/-
		DPC-DUN (TIP 2023) [53]	26.95/0.8357	32.34/0.9319	33.50/0.9466	35.55/0.9620	37.48/0.9734	33.16/0.9299
		OCTUF (CVPR 2023) [55]	27.76/0.8622	32.96/0.9444	34.18/0.9553	36.22/0.9696	38.23/0.9794	33.87/0.9422
		NesTD-Net (TIP 2024) [19]	27.74/0.8673	32.94/0.9444	33.44/0.9513	35.87/0.9680	-/-	-/-
		UFC-Net (CVPR 2024) [65]	27.54/0.8581	32.81/0.9421	-/-	-/-	-/-	-/-
		CPP-Net (CVPR 2024) [24]	28.48/0.8798	33.37/0.9483	34.56/0.9583	36.48/0.9712	38.29/0.9799	34.24/0.9475
		CASNet (TIP 2022) [2]	27.43/0.8613	32.20/0.9394	33.36/0.9510	35.45/0.9667	37.43/0.9770	33.17/0.9391
		AMS-Net (TMM 2022) [75]	28.04/0.8398	33.22/0.9326	34.35/0.9451	36.38/0.9614	38.33/0.9716	34.06/0.9301
		Uformer-ICS (TSC 2023) [76]	29.10/0.8589	33.87/0.9353	35.02/0.9464	37.11/0.9617	39.06/0.9720	34.83/0.9349
SIB-ACS (ours)	29.70/0.8859	35.15/0.9516	36.50/0.9605	38.93/0.9727	41.28/0.9807	36.31/0.9503		

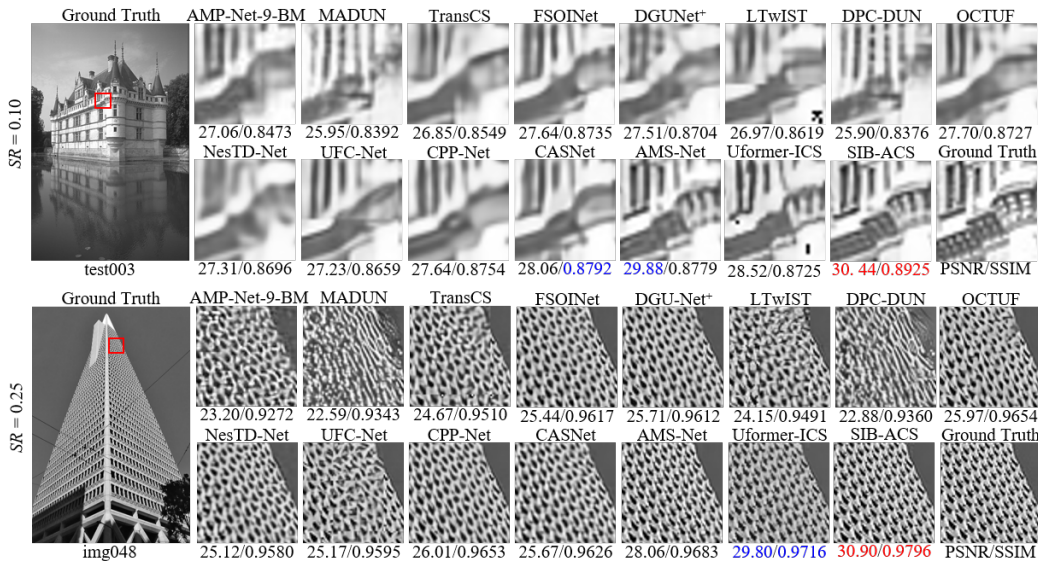


Figure 4. Visual comparisons of reconstructed image on test003 from BSD68 [37] at the sampling ratio of 0.10 and img048 from Urban100 [33] at the sampling ratio of 0.25. The best and second-best results are marked in red and blue colors, respectively.

implementation details and supplementary experiments can be found in the *Supplementary Material*.

4.2. Comparison with the state-of-the-arts

We perform multiple qualitative comparison experiments between the proposed SIB-ACS and the recent state-of-the-art CS models [2, 7, 18, 19, 24, 41, 45, 52, 53, 55, 65, 75–77] at sampling rates of 0.10, 0.25, 0.30, 0.40, and 0.50, as shown in Tab. 1. The results show that the proposed SIB-ACS significantly sur-

passes existing advanced models in terms of image fidelity. The average PSNR(dB)/SSIM of the proposed SIB-ACS exceeds the second-best model on the BSD68 and Urban100 datasets by 1.10(3.17%)/0.0101(1.10%) and 1.48(4.25%)/0.0028(0.30%) respectively, evidencing the high-fidelity scene sensing capabilities of SIB-ACS.

Furthermore, we conduct visual comparisons of the proposed SIB-ACS with the recent state-of-the-art models on the BSD68 [37] and Urban100 [33] datasets at sampling rates of 0.10 and 0.25, as depicted in Fig. 4. As can be

observed from Fig. 4, under various test dataset and sampling rate conditions, the proposed SIB-ACS is capable of more effectively identifying difficult-to-reconstruct areas in images and adaptively allocating sampling, which results in superior visual outcomes in the reconstruction of complex image areas, thereby enhancing the overall visual quality of the image.

4.3. Effectiveness of ASM

Table 2. PSNR (dB) and SSIM comparisons of Uniform Sampling (US) and Adaptive Sampling (AS). The best results is marked in bold.

Sampling module	BSD68		Urban100	
	$SR = 0.10$	$SR = 0.25$	$SR = 0.10$	$SR = 0.25$
US	28.38/0.8207	32.15/0.9172	28.69/0.8807	33.11/0.9463
AS	29.54/0.8401	34.35/0.9312	29.70/0.8850	35.15/0.9516

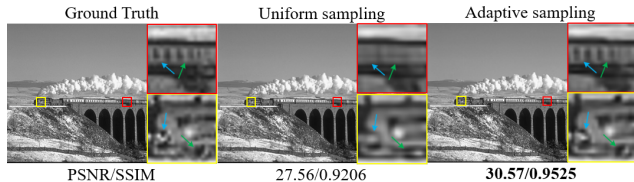


Figure 5. Visual comparisons of Uniform Sampling (US) and Adaptive Sampling (AS) on test033 from BSD68 at the sampling ratio of 0.25.

Effectiveness of Adaptive Sampling. We conduct comparative experiments between adaptive sampling (AS) and uniform sampling (US) to evaluate the effectiveness of AS, as presented in Tab. 2. US performs the same number of samples for each image block, while the proposed AS method adjusts the number of samples per image block based on the block’s innovation. Both types of sampling use the same reconstruction network for image reconstruction. The results in Tab. 2 show that compared to US, AS significantly improves the overall sensing ability of the image. Furthermore, we perform visual comparisons of the reconstruction results, as illustrated in Fig. 5. The visual quality of the reconstructed images suggest that, compared to US, the AS method can enhance sensing in areas with complex details, thereby improving the overall quality of image reconstruction.

Table 3. PSNR (dB) and SSIM comparisons of different Adaptive Sampling (AS) methods. The best results is marked in bold.

AS methods	BSD68		Urban100	
	$SR = 0.10$	$SR = 0.25$	$SR = 0.10$	$SR = 0.25$
Measurement Error	28.47/0.8124	32.63/0.9119	28.95/0.8732	34.16/0.9444
Saliency	28.50/0.8169	32.59/0.9141	28.40/0.8715	33.71/0.9448
Sampling Innovation	29.54/0.8401	34.35/0.9312	29.70/0.8850	35.15/0.9516

Effectiveness of Innovation Criterion. We compare the reconstruction results and the ASA results at each stage of the innovation-guided ACS framework with those of

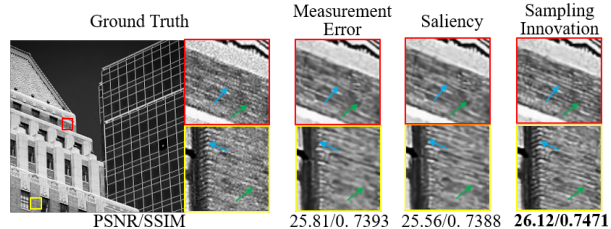


Figure 6. Visual comparisons of reconstructed image on img063 from Urban100 [33] at the sampling ratio of 0.25 using different AS methods.

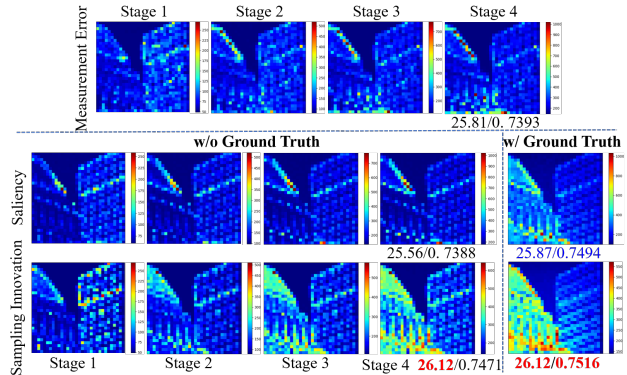


Figure 7. Visualization of sampling distribution at each stage in a multi-stage AS framework using different AS methods.

the measurement error [28, 43] and saliency [2, 71, 76], as depicted in Tab. 3 and Figs. 6 and 7 respectively. Table. 3 and Fig. 6 indicate that the innovation-guided multi-stage AS framework yields the best image reconstruction results. As illustrated in Fig. 7, the saliency-guided multi-stage ACS framework exhibits a positive feedback characteristic, where areas with high initial reconstruction saliency tend to accumulate samples, making it challenging to correct the ASA errors in areas that have high saliency in the original image but low initial reconstruction quality. The measurement error-guided multi-stage ACS framework has a negative feedback characteristic, capable of progressively correcting ASA errors. However, due to the influence of error clamping [28, 43], the measurement error-guided model still exhibits non-negligible ASA errors in the end. Compared to the image-domain-based saliency ASA method, the innovation-guided ASA method exhibits negative feedback characteristics. Because innovation utilizes sampling increment information, a relative measure, which can reflect which image blocks’ principal components have been restored as AS progresses and guides the ASA towards other image blocks that require more sampling, thereby progressively correcting the ASA. Simultaneously, compared to measurement error, because innovation is based on reconstructed image metrics, which contain richer image data information, the innovation-guided ASA possesses higher accuracy. In summary, the proposed innovation criterion is effective for guiding high-accuracy ASA.

4.4. Effectiveness of PCCD-Net

Table 4. Ablation experiments of PCPGD and CDPGD. The PC-Net and CD-Net are derived from the PCCD-Net by respectively omitting the CDPGD and PCPGD paths. The best results is marked in bold.

Models	PCPGD	CDPGD	BSD68		Urban100	
			$SR = 0.10$	$SR = 0.25$	$SR = 0.10$	$SR = 0.25$
PC-Net	✓	×	28.32/0.8197	32.11/0.9169	28.37/0.8759	32.94/0.9452
CD-Net	×	✓	28.22/0.8171	32.10/0.9166	28.10/0.8710	32.83/0.9438
PCCD-Net	✓	✓	28.38/0.8207	32.15/0.9172	28.69/0.8807	33.11/0.9463

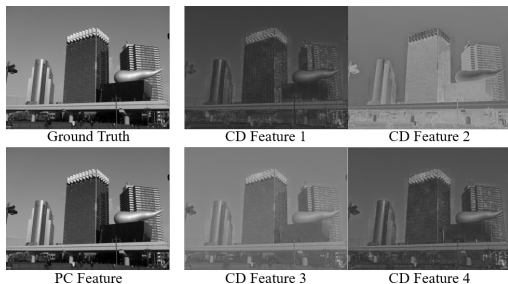


Figure 8. Visualization of principal component (PC) image in PCPGD and compressed domain (CD) features in CDPGD.

Ablation of PCPGD and CDPGD. To verify the contributions of PCPGD and CDPGD to the PCCD-Net, we conduct corresponding ablation experiments, as depicted in Tab. 4. The results indicate that the removal of CDPGD and PCPGD from PCCD-Net leads to varying degrees of decline in reconstruction performance, demonstrating the effectiveness of CDPGD and PCPGD. To ensure that the performance improvement is not merely due to the larger model parameters in PCCD-Net, more detailed convergence verification is provided in the *Supplementary Material*. Additionally, we visualize the features undergoing the PGD operation in CDPGD and PCPGD, as illustrated in Fig. 8. The visualization results confirm that PCPGD executes the PGD of the principal component image, while CDPGD carries out the PGD of the supplementary features in the compressed domain, ultimately achieving high-quality reconstruction of image features.

Table 5. Ablation experiments of compressed domain (CD) dimension. The best results is marked in bold.

CD Dimension	BSD68		Urban100		MACs (T)	
	$SR = 0.10$	$SR = 0.25$	$SR = 0.10$	$SR = 0.25$	$SR = 0.25$	$SR = 1.00$
2	28.30/0.8191	32.12/0.9169	28.51/0.8783	32.93/0.9451	1.4	5.2
4	28.38/0.8207	32.15/0.9172	28.69/0.8807	33.11/0.9463	2.2	8.5
8	28.38/0.8205	32.19/0.9178	28.65/0.8798	33.14/0.9467	3.9	15.1
16	28.33/0.8202	32.16/0.9175	28.54/0.8789	33.16/0.9471	7.2	28.3
32	28.32/0.8198	32.19/0.9178	28.51/0.8788	33.19/0.9471	13.8	54.7

Ablation of Compressed Domain (CD) Dimension. We investigate the performance of PCCD-Net with varying CD dimensions. When the CD dimensions are set to 2, 4, 8, 16, and 32 respectively, the reconstruction quality and Multiply-Accumulate Operations (MACs) of PCCD-Net are presented in Tab. 5. The results indicate an proportional increase in the model’s computational load corre-

sponding to the rise in feature and sampling matrix dimensions during the gradient descent operation. In ACS scenarios, which are typically characterized by a high upper limit of the block image sampling rate, careful design is required to manage the computational load introduced by the gradient descent operation. We observe an oscillation in the image reconstruction performance when the CD dimension exceeds 4. Considering both the reconstruction quality and computational load, we choose a CD dimension of 4.

4.5. Complexity Analysis

Table 6. Comparisons of the model average PSNR, parameter size, and running time. The best results is marked in bold.

Models	OCTUF	NesTD-Net	UFC-Net	CPP-Net	CASNet	PCCD-Net	SIB-ACS
PSNR (dB)	30.31	30.32	30.01	30.63	30.09	30.58	32.19
Params (M)	0.29	5.93	1.90	12.47	15.85	2.32	4.73
Time (s)	0.061	0.196	0.166	0.193	0.106	0.060	0.160

Computational complexity is a crucial reference indicator for model application. We evaluate the comprehensive performance of the proposed ACS model SIB-ACS and UCS model PCCD-Net by comparing the reconstruction quality, model parameter size, and runtime with state-of-the-art methods, as depicted in Tab. 6. The PSNR in Tab. 5 represents the average PSNR of the BSD68 [37] and Urban100 [33] datasets under sampling rates of 0.10 and 0.25. We measure the runtime by obtaining sampling values at a sampling rate of 0.25 on 256×256 images and then reconstructing the images. The results indicate that the runtime of the proposed PCCD-Net is comparable to that of the lightweight OCTUF [55], but the image reconstruction quality of PCCD-Net surpasses that of OCTUF. The image reconstruction quality of the proposed PCCD-Net is second only to CPP-Net [24], but the model parameters and runtime of PCCD-Net are significantly less than those of CPP-Net. Furthermore, under conditions of comparable model parameter size and runtime, the proposed ACS model SIB-ACS achieves the highest fidelity in image reconstruction.

5. Conclusion

In this paper, we propose a sampling innovation-based adaptive compressive sensing (SIB-ACS) framework that leverages image increment information for negative feedback to facilitate adaptive sampling allocation (ASA), achieving high-fidelity image reconstruction. The innovation criterion is proposed to adjudicate the ASA, and an innovation-guided multi-stage ASA framework is established to correct the ASA stage by stage. In addition, the proposed Principal Component Compressed Domain Network (PCCD-Net) ensures high-fidelity image reconstruction while controlling the computational burden of the gradient descent in the ACS scenario. Extensive experiments have confirmed the effectiveness of the proposed SIB-ACS and its capability to reconstruct high-fidelity scenes.

References

- [1] Marc A β mann and Manfred Bayer. Compressive adaptive computational ghost imaging. *Scientific reports*, 3(1):1545, 2013. 2
- [2] Bin Chen and Jian Zhang. Content-aware scalable deep compressed sensing. *IEEE Transactions on Image Processing*, 31:5412–5426, 2022. 2, 6, 7
- [3] Bin Chen, Jiechong Song, Jingfen Xie, and Jian Zhang. Deep physics-guided unrolling generalization for compressed sensing. *International Journal of Computer Vision*, 131(11):2864–2887, 2023. 3
- [4] Bin Chen, Xuanyu Zhang, Shuai Liu, Yongbing Zhang, and Jian Zhang. Self-supervised scalable deep compressed sensing. *International Journal of Computer Vision*, pages 1–36, 2024. 3
- [5] Bin Chen, Zhenyu Zhang, Weiqi Li, Chen Zhao, Jiwen Yu, Shijie Zhao, Jie Chen, and Jian Zhang. Invertible diffusion models for compressed sensing. *arXiv preprint arXiv:2403.17006*, 2024. 3
- [6] Jiwei Chen, Yubao Sun, Qingshan Liu, and Rui Huang. Learning memory augmented cascading network for compressed sensing of images. In *European Conference on Computer Vision*, pages 513–529. Springer, 2020. 3
- [7] Wenjun Chen, Chunling Yang, and Xin Yang. Fsoinet: feature-space optimization-inspired network for image compressive sensing. In *Proceedings of the IEEE International Conference on Acoustics, Speech and Signal Processing (ICASSP)*, 2022. 6
- [8] Patrick L Combettes and Valérie R Wajs. Signal recovery by proximal forward-backward splitting. *Multiscale modeling & simulation*, 4(4):1168–1200, 2005. 4
- [9] Wenxue Cui, Shaohui Liu, and Debin Zhao. Fast hierarchical deep unfolding network for image compressed sensing. In *Proceedings of the 30th ACM International Conference on Multimedia (ACM MM)*, 2022. 3
- [10] Wenxue Cui, Xiaopeng Fan, Jian Zhang, and Debin Zhao. Deep unfolding network for image compressed sensing by content-adaptive gradient updating and deformation-invariant non-local modeling. *IEEE Transactions on Multimedia*, 2023. 3
- [11] Wenxue Cui, Shaohui Liu, Feng Jiang, and Debin Zhao. Image compressed sensing using non-local neural network. *IEEE Transactions on Multimedia*, 25:816–830, 2023. 3
- [12] Wenxue Cui, Xingtao Wang, Xiaopeng Fan, Shaohui Liu, Chen Ma, and Debin Zhao. G2-dun: Gradient guided deep unfolding network for image compressive sensing. In *Proceedings of the 31st ACM International Conference on Multimedia*, pages 7933–7942, 2023. 3
- [13] Zvi Devir and Michael Lindenbaum. Blind adaptive sampling of images. *IEEE Transactions on Image Processing*, 21(4):1478–1487, 2011. 2
- [14] Noam Elata, Tomer Michaeli, and Michael Elad. Adaptive compressed sensing with diffusion-based posterior sampling. In *European Conference on Computer Vision*, pages 290–308. Springer, 2025. 1, 2
- [15] Zi-En Fan, Feng Lian, and Jia-Ni Quan. Global sensing and measurements reuse for image compressed sensing. In *Proceedings of the IEEE/CVF Conference on Computer Vision and Pattern Recognition (CVPR)*, pages 8954–8963, 2022. 3
- [16] Hongping Gan, Yang Gao, Chunyi Liu, Haiwei Chen, Tao Zhang, and Feng Liu. Autobcs: Block-based image compressive sensing with data-driven acquisition and noniterative reconstruction. *IEEE Transactions on Cybernetics*, 53(4):2558–2571, 2021. 3
- [17] Hongping Gan, Minghe Shen, Yi Hua, Chunyan Ma, and Tao Zhang. From patch to pixel: A transformer-based hierarchical framework for compressive image sensing. *IEEE Transactions on Computational Imaging*, 9:133–146, 2023. 3
- [18] Hongping Gan, Xiaoyang Wang, Lijun He, and Jie Liu. Learned two-step iterative shrinkage thresholding algorithm for deep compressive sensing. *IEEE Transactions on Circuits and Systems for Video Technology*, 2023. 6
- [19] Hongping Gan, Zhen Guo, and Feng Liu. Nestd-net: Deep nestd-inspired unfolding network with dual-path deblocking structure for image compressive sensing. *IEEE Transactions on Image Processing*, 2024. 6
- [20] Zhihua Gan, Xiuli Chai, Jianqiang Bi, and Xiuhui Chen. Content-adaptive image compression and encryption via optimized compressive sensing with double random phase encoding driven by chaos. *Complex & Intelligent Systems*, 8(3):2291–2309, 2022. 1
- [21] Kuiliang Gao, Bing Liu, Xuchu Yu, and Anzhu Yu. Unsupervised meta learning with multiview constraints for hyperspectral image small sample set classification. *IEEE Transactions on Image Processing*, 31:3449–3462, 2022. 3
- [22] Kuiliang Gao, Anzhu Yu, Xiong You, Wenyue Guo, Ke Li, and Ningbo Huang. Integrating multiple sources knowledge for class asymmetry domain adaptation segmentation of remote sensing images. *IEEE Transactions on Geoscience and Remote Sensing*, 62:1–18, 2024. 3
- [23] Davis Gilton, Greg Ongie, and Rebecca Willett. Neumann networks for linear inverse problems in imaging. *IEEE Transactions on Computational Imaging*, 6:328–343, 2019. 3
- [24] Zhen Guo and Hongping Gan. Cpp-net: Embracing multi-scale feature fusion into deep unfolding cp-ppa network for compressive sensing. In *Proceedings of the IEEE/CVF Conference on Computer Vision and Pattern Recognition*, pages 25086–25095, 2024. 6, 8
- [25] Jürgen Hahn, Christian Debes, Michael Leigsnering, and Abdelhak M Zoubir. Compressive sensing and adaptive direct sampling in hyperspectral imaging. *Digital Signal Processing*, 26:113–126, 2014. 1, 2
- [26] Kai Han, Jin Wang, Yunhui Shi, Nam Ling, and Baocai Yin. D3u-net: Dual-domain collaborative optimization deep unfolding network for image compressive sensing. In *Proceedings of the 32nd ACM International Conference on Multimedia*, pages 9952–9960, 2024. 3
- [27] Yujun Huang, Bin Chen, Naiqi Li, Baoyi An, Shu-Tao Xia, and Yaowei Wang. Mb-racs: Measurement-bounds-based rate-adaptive image compressed sensing network. *arXiv preprint arXiv:2402.16855*, 2024. 1, 2
- [28] Chen Hui, Shengping Zhang, Wenxue Cui, Shaohui Liu, Feng Jiang, and Debin Zhao. Rate-adaptive neural network

- for image compressive sensing. *IEEE Transactions on Multimedia*, pages 1–15, 2023. 1, 2, 7
- [29] Chen Hui, Haiqi Zhu, Shuya Yan, Shaohui Liu, Feng Jiang, and Debin Zhao. S2-csnet: Scale-aware scalable sampling network for image compressive sensing. In *Proceedings of the 32nd ACM International Conference on Multimedia*, pages 2515–2524, 2024. 3
- [30] Hongzhi Jiang, Shuguang Zhu, Huijie Zhao, Bingjie Xu, and Xudong Li. Adaptive regional single-pixel imaging based on the fourier slice theorem. *Optics express*, 25(13):15118–15130, 2017. 1
- [31] Xiaoyu Kong, Yongyong Chen, and Zhenyu He. When channel correlation meets sparse prior: Keeping interpretability in image compressive sensing. *IEEE Transactions on Multimedia*, 2023. 1, 3
- [32] Alexandros Kontogiannis and Matthew P Juniper. Physics-informed compressed sensing for pc-mri: an inverse navier-stokes problem. *IEEE Transactions on Image Processing*, 32:281–294, 2022. 1
- [33] Wei-Sheng Lai, Jia-Bin Huang, Narendra Ahuja, and Ming-Hsuan Yang. Fast and accurate image super-resolution with deep laplacian pyramid networks. *IEEE transactions on pattern analysis and machine intelligence*, 41(11):2599–2613, 2018. 1, 6, 7, 8
- [34] Tiancheng Li, Qiorong Yan, Quan Zou, and Qianling Dai. Gates-controlled deep unfolding network for image compressed sensing. *IEEE Transactions on Computational Imaging*, 2024. 3
- [35] Weiqi Li, Bin Chen, Shuai Liu, Shijie Zhao, Bowen Du, Yongbing Zhang, and Jian Zhang. D 3 c 2-net: Dual-domain deep convolutional coding network for compressive sensing. *IEEE Transactions on Circuits and Systems for Video Technology*, 2024. 3
- [36] Lijing Ma, Huihui Bai, Mengmeng Zhang, and Yao Zhao. Edge-based adaptive sampling for image block compressive sensing. *IEICE TRANSACTIONS on Fundamentals of Electronics, Communications and Computer Sciences*, 99(11):2095–2098, 2016. 2
- [37] David Martin, Charless Fowlkes, Doron Tal, and Jitendra Malik. A database of human segmented natural images and its application to evaluating segmentation algorithms and measuring ecological statistics. In *Proceedings Eighth IEEE International Conference on Computer Vision. ICCV 2001*, pages 416–423. IEEE, 2001. 1, 6, 8
- [38] R Monika and Samiappan Dhanalakshmi. An efficient medical image compression technique for telemedicine systems. *Biomedical Signal Processing and Control*, 80:104404, 2023. 1
- [39] R Monika, Samiappan Dhanalakshmi, R Kumar, and R Narayanamoorthi. Coefficient permuted adaptive block compressed sensing for camera enabled underwater wireless sensor nodes. *IEEE Sensors Journal*, 22(1):776–784, 2021. 2
- [40] R Monika, Dhanalakshmi Samiappan, and R Kumar. Underwater image compression using energy based adaptive block compressive sensing for iout applications. *The Visual Computer*, 37(6):1499–1515, 2021. 2
- [41] Chong Mou, Qian Wang, and Jian Zhang. Deep generalized unfolding networks for image restoration. In *Proceedings of the IEEE/CVF Conference on Computer Vision and Pattern Recognition (CVPR)*, 2022. 3, 6
- [42] Yan Qian, Ruiqing He, Qian Chen, Guohua Gu, Feng Shi, and Wenwen Zhang. Adaptive compressed 3d ghost imaging based on the variation of surface normals. *Optics Express*, 27(20):27862–27872, 2019. 2
- [43] Chenxi Qiu and Xuemei Hu. Adacs: Adaptive compressive sensing with restricted isometry property-based error-clamping. *IEEE Transactions on Pattern Analysis and Machine Intelligence*, 2024. 1, 2, 5, 7
- [44] Chenxi Qiu, Tao Yue, and Xuemei Hu. Reconstruction-free cascaded adaptive compressive sensing. In *Proceedings of the IEEE/CVF Conference on Computer Vision and Pattern Recognition*, pages 2620–2630, 2024. 1, 2, 5
- [45] Minghe Shen, Hongping Gan, Chao Ning, Yi Hua, and Tao Zhang. Transcs: a transformer-based hybrid architecture for image compressed sensing. *IEEE Transactions on Image Processing*, 31:6991–7005, 2022. 6
- [46] Wuzhen Shi, Feng Jiang, Shaohui Liu, and Debin Zhao. Image compressed sensing using convolutional neural network. *IEEE Transactions on Image Processing*, 29:375–388, 2019. 3
- [47] Wuzhen Shi, Feng Jiang, Shaohui Liu, and Debin Zhao. Scalable convolutional neural network for image compressed sensing. In *Proceedings of the IEEE/CVF Conference on Computer Vision and Pattern Recognition (CVPR)*, pages 12290–12299, 2019. 3
- [48] Yuandi Shi, Rongrong Chen, Donglin Liu, and Bin Wang. A visually secure image encryption scheme based on adaptive block compressed sensing and non-negative matrix factorization. *Optics & Laser Technology*, 163:109345, 2023. 1
- [49] Fernando Soldevila, Eva Salvador-Balaguer, P Clemente, Enrique Tajahuerce, and Jesús Lancis. High-resolution adaptive imaging with a single photodiode. *Scientific reports*, 5(1):14300, 2015. 1, 2
- [50] Heping Song, Jingyao Gong, Hongying Meng, and Yuping Lai. Multi-cross sampling and frequency-division reconstruction for image compressed sensing. In *Proceedings of the AAAI Conference on Artificial Intelligence*, pages 4909–4917, 2024. 3
- [51] Jiechong Song and Jian Zhang. Sodas-net: Side-information-aided deep adaptive shrinkage network for compressive sensing. *IEEE Transactions on Instrumentation and Measurement*, 72:1–12, 2023. 3
- [52] Jiechong Song, Bin Chen, and Jian Zhang. Memory-augmented deep unfolding network for compressive sensing. In *Proceedings of the 29th ACM international conference on multimedia (ACM MM)*, pages 4249–4258, 2021. 6
- [53] Jiechong Song, Bin Chen, and Jian Zhang. Dynamic path-controllable deep unfolding network for compressive sensing. *IEEE Transactions on Image Processing*, 32:2202–2214, 2023. 6
- [54] Jiechong Song, Bin Chen, and Jian Zhang. Deep memory-augmented proximal unrolling network for compressive sensing. *International Journal of Computer Vision*, 131(6):1477–1496, 2023. 3
- [55] Jiechong Song, Chong Mou, Shiqi Wang, Siwei Ma, and Jian Zhang. Optimization-inspired cross-attention transformer

- for compressive sensing. In *Proceedings of the IEEE/CVF Conference on Computer Vision and Pattern Recognition (CVPR)*, pages 6174–6184, 2023. 5, 6, 8
- [56] Rayko I Stantchev, David B Phillips, Peter Hobson, Samuel M Hornett, Miles J Padgett, and Euan Hendry. Compressed sensing with near-field thz radiation. *Optica*, 4(8): 989–992, 2017. 1, 2
- [57] Rayko I Stantchev, David B Phillips, Peter Hobson, Samuel M Hornett, Miles J Padgett, and Euan Hendry. Compressed sensing with near-field thz radiation. *Optica*, 4(8): 989–992, 2017. 2
- [58] Yueming Su and Qiusheng Lian. ipiano-net: Nonconvex optimization inspired multi-scale reconstruction network for compressed sensing. *Signal Processing: Image Communication*, 89:115989, 2020. 3
- [59] Yubao Sun, Jiwei Chen, Qingshan Liu, Bo Liu, and Guodong Guo. Dual-path attention network for compressed sensing image reconstruction. *IEEE Transactions on Image Processing*, 29:9482–9495, 2020. 3
- [60] Ali Taimori and Farokh Marvasti. Adaptive sparse image sampling and recovery. *IEEE Transactions on Computational Imaging*, 4(3):311–325, 2018. 2
- [61] Jianming Wang, Wei Wang, and Jianhua Chen. Adaptive rate block compressive sensing based on statistical characteristics estimation. *IEEE transactions on image processing*, 31:734–747, 2021. 1, 2
- [62] Ping Wang and Xin Yuan. Saunet: Spatial-attention unfolding network for image compressive sensing. In *Proceedings of the 31st ACM International Conference on Multimedia*, pages 5099–5108, 2023. 1, 3
- [63] Wei Wang and Jianhua Chen. Adaptive rate image compressive sensing based on the hybrid sparsity estimation model. *Digital Signal Processing*, 139:104079, 2023. 2
- [64] Wei Wang, Jianhua Chen, and Yufeng Zhang. Adaptive compressive sensing based on sparsity order estimation for wireless image sensor networks. *IEEE Sensors Journal*, 2024. 1, 2
- [65] Xiaoyang Wang and Hongping Gan. Ufc-net: Unrolling fixed-point continuous network for deep compressive sensing. In *Proceedings of the IEEE/CVF Conference on Computer Vision and Pattern Recognition*, pages 25149–25159, 2024. 6
- [66] Jian Yang, Haixin Wang, Ittetsu Taniguchi, Yibo Fan, and Jinjia Zhou. avcsr: Adaptive video compressive sensing using region-of-interest detection in the compressed domain. *IEEE MultiMedia*, 2023. 2
- [67] Yan Yang, Jian Sun, Huibin Li, and Zongben Xu. Admm-csnet: A deep learning approach for image compressive sensing. *IEEE transactions on pattern analysis and machine intelligence*, 42(3):521–538, 2018. 3
- [68] Hantao Yao, Feng Dai, Shiliang Zhang, Yongdong Zhang, Qi Tian, and Changsheng Xu. Dr2-net: Deep residual reconstruction network for image compressive sensing. *Neurocomputing*, 359:483–493, 2019. 3
- [69] Dongjie Ye, Zhangkai Ni, Hanli Wang, Jian Zhang, Shiqi Wang, and Sam Kwong. Csformer: Bridging convolution and transformer for compressive sensing. *IEEE Transactions on Image Processing*, 32:2827–2842, 2023. 3, 5
- [70] Wen-Kai Yu, Ming-Fei Li, Xu-Ri Yao, Xue-Feng Liu, Ling-An Wu, and Guang-Jie Zhai. Adaptive compressive ghost imaging based on wavelet trees and sparse representation. *Optics express*, 22(6):7133–7144, 2014. 2
- [71] Ying Yu, Bin Wang, and Liming Zhang. Saliency-based compressive sampling for image signals. *IEEE signal processing letters*, 17(11):973–976, 2010. 2, 7
- [72] Jian Zhang and Bernard Ghanem. Ista-net: Interpretable optimization-inspired deep network for image compressive sensing. In *Proceedings of the IEEE conference on computer vision and pattern recognition (CVPR)*, pages 1828–1837, 2018. 3
- [73] Jian Zhang, Zhenyu Zhang, Jingfen Xie, and Yongbing Zhang. High-throughput deep unfolding network for compressive sensing mri. *IEEE Journal of Selected Topics in Signal Processing*, 16(4):750–761, 2022. 3
- [74] Jian Zhang, Bin Chen, Ruiqin Xiong, and Yongbing Zhang. Physics-inspired compressive sensing: Beyond deep unrolling. *IEEE Signal Processing Magazine*, 40(1):58–72, 2023. 3
- [75] Kuiyuan Zhang, Zhongyun Hua, Yuanman Li, Yongyong Chen, and Yicong Zhou. Ams-net: Adaptive multi-scale network for image compressive sensing. *IEEE Transactions on Multimedia*, 25:5676–5689, 2023. 6
- [76] Kuiyuan Zhang, Zhongyun Hua, Yuanman Li, Yushu Zhang, and Yicong Zhou. Uformer-ics: A u-shaped transformer for image compressive sensing service. *IEEE Transactions on Services Computing*, 2023. 1, 2, 3, 6, 7
- [77] Zhonghao Zhang, Yipeng Liu, Jiani Liu, Fei Wen, and Ce Zhu. Amp-net: Denoising-based deep unfolding for compressive image sensing. *IEEE Transactions on Image Processing*, 30:1487–1500, 2020. 6
- [78] Hang Zhao, Orazio Gallo, Iuri Frosio, and Jan Kautz. Loss functions for image restoration with neural networks. *IEEE Transactions on computational imaging*, 3(1):47–57, 2016. 5
- [79] Yuanhong Zhong, Chenxu Zhang, Fan Ren, Honggang Kuang, and Panliang Tang. Scalable image compressed sensing with generator networks. *IEEE Transactions on Computational Imaging*, 8:1025–1037, 2022. 3
- [80] Siwang Zhou, Yan He, Yonghe Liu, Chengqing Li, and Jianming Zhang. Multi-channel deep networks for block-based image compressive sensing. *IEEE Transactions on Multimedia*, 23:2627–2640, 2020. 1
- [81] Shuyuan Zhu, Bing Zeng, and Moncef Gabbouj. Adaptive sampling for compressed sensing based image compression. *Journal of Visual Communication and Image Representation*, 30:94–105, 2015. 2
- [82] Lihao Zhuang, Liquan Shen, Zhengyong Wang, and Yinyi Li. Ucsnet: Priors guided adaptive compressive sensing framework for underwater images. *IEEE Transactions on Circuits and Systems for Video Technology*, 2023. 1, 2